

Friction at ice-I_h / water interfaces is governed by solid-liquid hydrogen-bonding

Patrick B. Louden and J. Daniel Gezelter*

Department of Chemistry and Biochemistry, University of Notre Dame, Notre Dame, IN 46556

E-mail: gezelter@nd.edu

Abstract

We present evidence that the surface density of solid to liquid hydrogen bonds directly correlates with the solid/liquid friction of ice/water interfaces. Using non-equilibrium molecular dynamics simulations, the basal {0001}, prismatic {10 $\bar{1}$ 0}, pyramidal {20 $\bar{2}$ 1}, and secondary prism {11 $\bar{2}$ 0} facets of ice-I_h were drawn through liquid water with a momentum flux between the solid and liquid phases. Solid to liquid hydrogen bonds were identified using local tetrahedral ordering of the water molecules. An expression for friction coefficients appropriate for negative slip boundary conditions is presented, and the computed friction of these interfaces is found to be invariant to the shear rate and direction of shear relative to the surface features. Structural and dynamic interfacial widths for all four facets were found to be similar, and are also independent of the shear rate and direction. Differences in the solid to liquid hydrogen bond density are explained in terms of surface features of the four facets.

Introduction

Ice friction has been investigated extensively with a range experiments to elucidate the role of temperature,^{1–6} sliding speed,^{2,4,5} applied load,^{1,4,7–9} contact area,^{1,10} and moisture.¹¹ Kietzig *et al.* performed experiments on steel alloy rings sliding over a prepared ice surface.¹² They investigated the effect of surface nanopatterning, hydrophobicity, and surface structure of the ice-exposed slider on the ice/slider friction. Using laser irradiation, the slider surface hydrophobicity was tuned without changing the chemical nature of the material. Kietzig showed that laser-induced hydrophobicity resulted in fewer capillary bridges forming between the slider and a thin film of melted ice. This reduced the amount of viscous shearing of the ice-melt, resulting in a lower friction coefficient. While ice friction experiments have focused on heterogeneous materials,^{1,2,4,5,9,10,12–14} there have also been significant advances made on understanding ice-ice friction.^{7,15–20}

Experiments and computer simulations both suggest the existence of a quasi-liquid layer (QLL) that forms at the surface of ice at temperatures below the bulk melting point but above 235K.^{21–26} The formation of this layer is driven by the termination of the periodic crystal structure. The surface

molecules are not as tightly bound to their lattice positions as molecules in the underlying ice, and with sufficient thermal energy, these molecules reorient to maximize hydrogen bonding. At warmer temperatures, they can also translate along the surface.^{25,27} The existence of the QLL is now generally accepted as one of the reasons that ice displays a low coefficient of sliding friction.^{28–31}

Generally, three distinct ice friction regimes have been found: boundary friction, mixed friction, and hydrodynamic friction, and the particular regime depends on the temperature and sliding velocity of the material.^{12,14,32–34} The observed friction is the result of different physical processes in each regime. In boundary friction, the lubricating layer of ice melt is only a few molecules thick. This thin film is unable to support the sliding load, and friction can be attributed to surface asperities of the sliding material interacting with the ice surface itself.³² In the mixed friction regime, the lubricating layer is thicker than in the boundary regime, but not yet sufficiently thick to maintain the sliding load. The QLL film reduces solid-solid adhesion at the interface, although the lubricating layer can also form capillary bridges with the material, resulting in a drag force.^{12,14}

If the liquid layer is thick enough to support the sliding load, the slider's surface asperities are no longer in contact with the surface and the observed friction may be due to the capillary bridges formed between the ice melt and the material. Under these conditions, the ice friction is classified as hydrodynamic friction.^{12,14} Thus the three regimes are characterized by the extent that a liquid-like layer of water mitigates the sliding load.

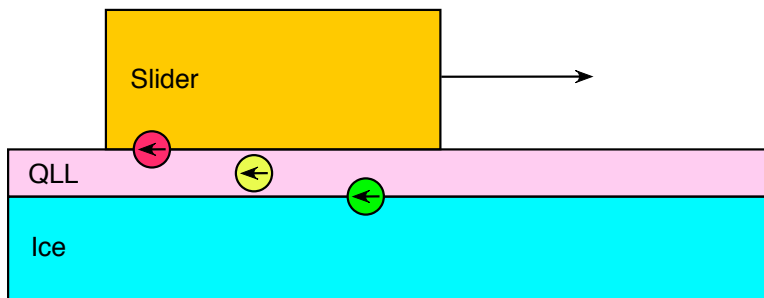


Figure 1: In the hydrodynamic regime, the friction felt by a slider on an ice surface is mediated by a quasi-liquid layer (QLL) that forms on the surface of the ice. There can be many contributions to this friction: capillary bridges between the material and the QLL (red), viscous drag in the liquid (yellow), and solid-liquid friction between the ice and the liquid film (green). This study concerns the last of the three contributions, the drag contributed by the ice-liquid interface.

Kietzig *et al.* have outlined popular experimental techniques used to investigate the coefficients of friction for a variety of materials sliding on ice, as well as their sensitivity to temperature, slider load, contact area, wettability and hydrophobicity of the slider.¹⁴ Of particular interest, the friction coefficients were found to increase with increasing slider velocity. This was attributed to three physical processes; adhesion forces between the slider's asperities and the ice surface, breaking of capillary bridges between the slider and the ice surface, and the viscous shearing of the ice melt across the ice surface. While teasing apart the individual contributions has proven challenging, Kietzig¹² and Persson^{33,34} have made significant progress. However, there is still very little known about water shearing over ice surfaces. Open questions include: how does the structure of the interface change during this process, and what role does the presented crystal facet have in the observed friction?

To help understand slider-ice friction in the hydrodynamic regime, we have simulated the drag forces contributed by the interaction of the liquid water film with the underlying ice facet. This study uses non-equilibrium molecular dynamics (with an applied momentum flux) to create a shear flow at the ice/water interface. The magnitude of the momentum flux is then used to compute the solid-liquid friction for four different facets of ice that are presented to the liquid. We have previously used this technique to study solid-liquid friction for the basal and prismatic crystal facets where we observed significant facet-dependence, and noted surface corrugations that could contribute to these differences.³⁵ Here, we broaden the investigation to four common ice facets, we study significantly larger systems for significantly longer times, a wider range of shear rates, and we introduce a novel method for calculating solid-liquid friction coefficients under conditions of *negative* slip.

Methodology

Construction of Ice / Water interfaces

Ice I_h crystallizes in the hexagonal space group P6₃/*mmc*, and ice crystals normally form hexagonal plates with the basal face, {0001}, forming the top and bottom of each plate, and the prismatic facet, {10̄10}, forming the sides. In extreme temperatures or low water saturation conditions, ice crystals can form hollow columns, needles, and dendrites, exposing other crystalline facets of the ice to the surroundings. Among the more commonly-observed facets are the secondary prism, {11̄20}, and pyramidal, {20̄21}, faces.

Although bulk ice I_h is proton disordered, our simulations were carried out with proton-ordered, zero-dipole crystals that expose stripes of dangling H-atoms and lone pairs. These initial configurations reproduce the surface features from Buch *et al.*³⁶ that helped interpret sum-frequency generation (SFG) experiments by the Schultz lab.³⁷ Our structures were created starting from Structure 6 of Hirsch and Ojamäe's set of orthorhombic representations for ice-I_h.³⁸ The primitive unit cell was replicated in all dimensions. The crystal was cleaved along the desired face, and two additional mutually perpendicular cuts were made. The crystal was reoriented so that the initial cut was normal to the *z*-axis of the simulation cell. The resulting structures were extended in *x* and *y* to form large exposed facets in rectangular box geometries.

Liquid water boxes were created with identical dimensions (in *x* and *y*) as the ice, with a *z* dimension of three times that of the ice block, and with a density corresponding to 1 g / cm³. Each of the ice slabs and water boxes were independently equilibrated to 50K and a pressure of 1 atm, and the resulting systems were merged by carving out any liquid water molecules within 3 Å of any atoms in the ice slabs. Each of the combined ice/water systems were then equilibrated to 225K, which is the liquid-ice coexistence temperature for SPC/E water.³⁹ The quiescent ice / water interfaces were then equilibrated for 10 ns, with 5 ns under a constant temperature (NVT) integrator set to the coexistence temperature (225K), followed by 5 ns under a microcanonical (NVE) integrator. During this time the ice was monitored for crystal growth or melting. We

observed no advancement of the ice interface into the liquid, and no loss of crystallinity of the ice. Reference 35 contains a more detailed explanation of the construction of similar ice/water interfaces. The resulting dimensions as well as the number of ice and liquid water molecules contained in each of these systems are shown in Table 1. Note that the water molecules are not restrained in any way - molecules that start in the liquid phase may exchange with the ice (and vice versa).

Table 1: Sizes of the ice/water shearing simulations.

Interface	N_{ice}	N_{liquid}	$L_x (\text{\AA})$	$L_y (\text{\AA})$	$L_z (\text{\AA})$
Basal $\{0001\}$	900	1846	23.87	35.83	98.64
Prismatic $\{10\bar{1}0\}$	3000	5464	35.95	35.65	205.77
Pyramidal $\{20\bar{2}1\}$	1216	2203	37.47	29.50	93.02
Secondary Prism $\{11\bar{2}0\}$	3840	8176	71.87	31.66	161.55

The SPC/E water model⁴⁰ has been extensively characterized over a wide range of liquid conditions,^{41,42} and its phase diagram has been well studied.^{43–46} With longer cutoff radii and careful treatment of electrostatics, SPC/E mostly avoids metastable crystalline morphologies like ice-*i*⁴⁶ and ice-B,⁴³ although Sanz *et al.* found that the stable polymorph for this model is likely ice-II at this temperature and 1 bar.⁴⁵ The free energies and melting points^{39,41,43–50} of various other crystalline polymorphs have also been calculated. Haymet *et al.* have studied quiescent ice-I_h/water interfaces using the SPC/E water model, and have seen structural and dynamic measurements of the interfacial width that agree well with both experimental results and more expensive water models, although the coexistence temperature for SPC/E is still well below the experimental melting point of real water.³⁹ Given the extensive data and speed of this model, it is a reasonable choice even though the temperatures required are somewhat lower than real ice / water interfaces.

Creating shear in molecular simulations

The velocity shearing and scaling variant of reverse nonequilibrium molecular dynamics (VSS-RNEMD)⁴² was employed to create shear in our simulation cells. This method performs a series

of simultaneous nonequilibrium exchanges of linear momentum and kinetic energy between two physically separated regions of the simulation cell. The system responds to this unphysical flux with velocity and temperature gradients. When VSS-RNEMD is applied to bulk liquids, transport properties like the shear viscosity, η , are easily extracted assuming a linear response between the applied flux, $j_z(p_x)$, and the resulting gradient,

$$j_z(p_x) = -\eta \left(\frac{\partial v_x}{\partial z} \right). \quad (1)$$

At interfaces between dissimilar materials, the same method can be used to extract *interfacial* transport properties (e.g. the hydrodynamic slip length or the interfacial thermal conductance). Because the individual VSS-RNEMD exchange moves conserve both total energy and linear momentum, the method can be “bolted on” to simulations in any ensemble. A more detailed explanation of VSS-RNEMD shearing simulations applied to ice / water interfaces can be found in our previous work.³⁵

All simulations were performed using OpenMD,^{51,52} with a time step of 2 fs and periodic boundary conditions in all three dimensions. When applicable, VSS-RNEMD moves were attempted every time step. This minimized the magnitude of individual momentum exchanges. For all simulations, electrostatics were handled using the damped-shifted force real-space electrostatic kernel.⁵³

Shearing at ice / water interfaces

The RNEMD exchanges that force the solid to shear through a surrounding liquid do measurable work on the system, and this work causes frictional heating at the interface. Close to the melting point of the solid, this frictional heating may result in melting of the crystal. We are interested in the structure and dynamics of the interface at the coexistence temperature. Therefore, in order to prevent melting of the ice phase, we have imposed a weak kinetic energy flux ($J_z \sim 2.0 \times 10^{-6}$ kcal mol⁻¹ Å⁻² fs⁻¹) normal to the interface. The resulting thermal gradients (< 10 K over the length

of the simulation box) were allowed to stabilize for 5 ns, and were found to be sufficient in keeping the interface within ± 1 K of the 225 K target during all shearing simulations.

Once thermal gradients had stabilized, linear momentum fluxes were imposed coincident with the kinetic energy flux. The resulting velocity gradients were allowed to stabilize for 1 ns before data collection began. Four successive 1 ns simulations were performed for each shear rate (varying from $0.5 \rightarrow 10.0 \text{ m s}^{-1}$). Configurations of the systems were stored every 1 ps, and statistics on the structure and dynamics were accumulated every 0.1 ps. Small variations in the measured interfacial widths between successive simulations were observed, but there was no indication of bulk melting or crystal growth. That is, no large scale changes in the positions of the top and bottom interfaces were observed during the simulations. A representative configuration of the solvated prismatic facet being sheared through liquid water is shown in Figure 2.

Results

Structural measures of interfacial width under shear

One of the open questions about ice / water interfaces is whether the thickness of the interfacial ‘slush’ layer depends on the facet of ice presented to the water. In the interfacial region, the water molecules are ordered differently than in either the solid or liquid phases, and also exhibit dynamics unique to their local structure. The width of this interfacial layer has been estimated by finding the distance over which structural order parameters or dynamic properties change from their bulk liquid values to those of the solid ice. The properties used to find interfacial widths have included the local density, the diffusion constant, and both translational and orientational order parameters.^{35,39,47,54–57}

Because the VSS-RNEMD method creates thermal and velocity gradients in the system, the momenta of the water molecules are perturbed, and order parameters that depend on translational motion may measure the momentum exchange and not physical properties of the interface. As a structural measure of the interface, we have used the local tetrahedral order parameter, which

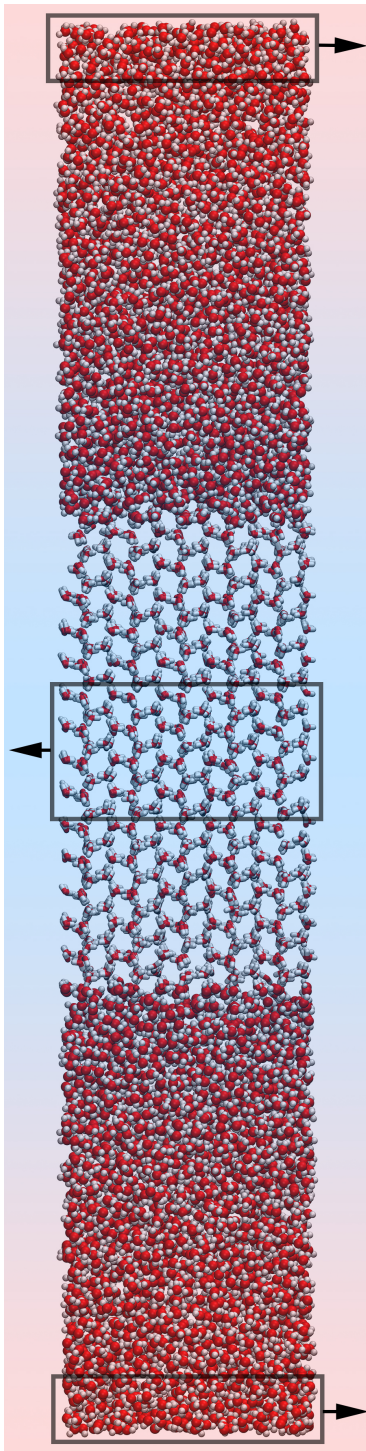


Figure 2: Computational model of a slab of ice being sheared through liquid water. The ice presents two copies of the prismatic $\{10\bar{1}0\}$ facet towards the liquid phase. The RNEMD simulation exchanges both linear momentum (indicated with arrows) and kinetic energy between the central box and the box that spans the cell boundary. The system responds with weak thermal gradient and a velocity profile that shears the ice relative to the surrounding liquid.

compares the local molecular environments (e.g. the angles between nearest neighbor molecules) to perfect tetrahedral ordering. This quantity was originally described by Chau and Hardwick,⁵⁸ was rescaled by Errington and Debenedetti,⁵⁹ and has been used in bulk liquid simulations by Kumar *et al.*⁶⁰ It has also previously been used in ice/water interfaces by Bryk and Haymet,⁴⁴ and in our initial work on ice / water interfaces.³⁵

We have evaluated the local tetrahedral order parameter, q , along the coordinate perpendicular to the ice / water interface, i.e., the z -axis of the simulation box.

$$q(z) = \frac{1}{N_z} \int_0^L \sum_{i=1}^N \left(1 - \frac{9}{2n(n-1)} \sum_{j=1}^{n-1} \sum_{k=j+1}^n \left(\cos \psi_{jik} + \frac{1}{3} \right)^2 \right) \delta(z_i - z) dz \quad (2)$$

ψ_{jik} is the angle formed between the oxygen sites of water molecules i , j , and k , where molecule i is the central water molecule and molecules j and k are two of the n neighbors of i . Molecules j and k lie within the first solvation shell of molecule i ($r < 3.41$ Å for water), and the double sum visits all angles for neighbors of molecule i that are within this distance. When molecule i has exactly four neighbors ($n = 4$), the prefactor reduces to $3/8$, as in the expression of Errington and Debenedetti, but Eq. (2) also provides tetrahedrality information for water molecules that are either under- or over-coordinated. We have also introduced the normalization factor $N_z = \sum_i \int \delta(z_i - z) dz$ to account for the varying populations of water molecules within each finite-width bin.

At low temperatures, the tetrahedral order parameter can approach unity for perfect ice-I_h structures. However, at temperatures close to melting, values of 0.9 are more common due to thermal motion in the lattice. In liquid water, overlap of the local environment with a perfect tetrahedron is reduced, and values of $q(z) \approx 0.75$ are common at 225 K.

The structural widths of the ice / water interfaces were determined by dividing each system into 1 Å bins along the z -axis, and computing statistical averages of $q(z)$ in each bin. For the secondary prism interface, the resulting distribution can be seen in the bottom panel of Fig. 3 (and in the Supporting Information for the other interfaces). In the bulk liquid (at small and large values of z), the order parameter takes on values of $q(z) \approx 0.77$, while $q(z) \approx 0.92$ was found in bins

spanning the ice. The tetrahedrality profiles were fit using a function that captures the smooth transition from the bulk liquid to ice (turquoise line in the bottom panel of the same figures),

$$q(z) \approx q_{\text{liq}} + \frac{q_{\text{ice}} - q_{\text{liq}}}{2} \left[\tanh\left(\frac{z-l}{w}\right) - \tanh\left(\frac{z-r}{w}\right) \right] + \beta \left| z - \frac{r+l}{2} \right|. \quad (3)$$

Here q_{liq} and q_{ice} are the values of the order parameter for the bulk liquid and ice domains. The locations l and r are the z -coordinates of the Gibbs dividing surface for the left and right interfaces (shown in Fig. 3 with vertical dotted lines), and w is the interfacial width. The last term in Eq. (3) accounts for the influence of the weak thermal gradient on the tetrahedrality profile in the liquid region. Namely, at warmer temperatures the liquid is able to adopt local configurations resulting in lower values of the order parameter. This results in a small linear decay in the tetrahedrality profiles for increasing displacements from the ice surface.

In the middle panel of Fig. 3, we show the resulting thermal gradient from the imposed kinetic energy flux. At the ice / water interface, the local temperature is held at approximately 225 K, allowing investigation of the response to the shear while maintaining solid-liquid coexistence. In the top panel, the velocity gradient resulting from the imposed momentum flux shows that the ice has a uniform positive velocity along the x axis. The bulk liquid at the ends of the simulation cell has negative velocity, although the center of mass of the simulation box is stationary. The bulk fluid shows a primarily linear velocity gradient allowing for easy calculation of the shear viscosity. Close to the interface, the ice imparts significant positive momentum into the surrounding interfacial liquid. Projections of the velocity gradient from the liquid onto the Gibbs dividing surface indicate that the ice-water interface is in the negative slip regime.

From Eq. (3), we have obtained estimates for w , the structural widths of the interfaces for the quiescent ice / water systems. These values are related to the 10% – 90% interfacial widths commonly reported in previous studies ($w_{10-90} = 2.197 w$).^{39,44} We find $w_{10-90} \approx 7 \text{ \AA}$ for each of the interfaces as seen in Table 2. These values are similar to our previous findings for the 10% – 90% interfacial widths obtained from shorter simulations, $(7.0 \pm 0.9 \text{ \AA})$ for the basal and $(7.9 \pm 0.4$

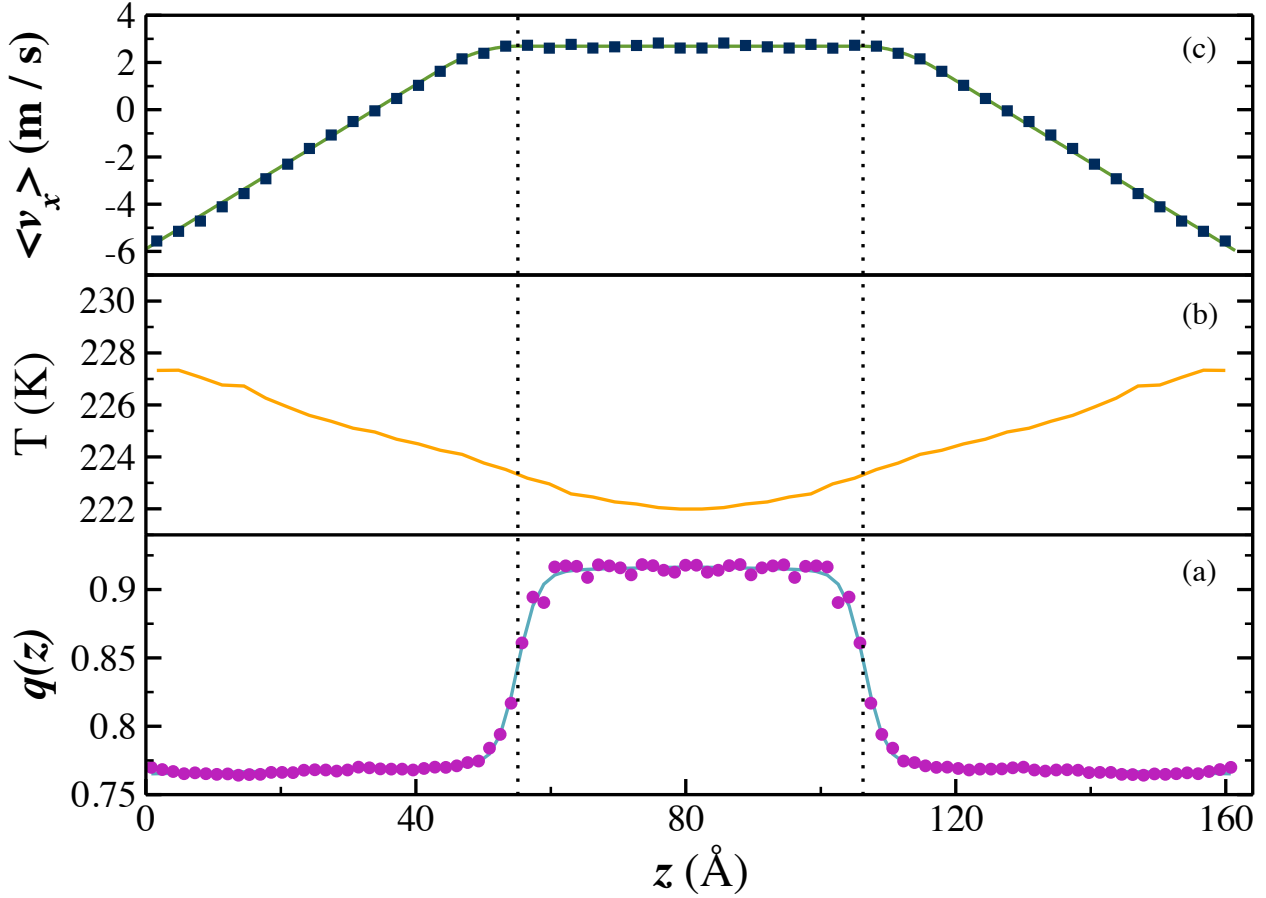


Figure 3: Properties of the secondary prism interface being sheared through water at 8.6 ms^{-1} . Lower panel: the local tetrahedral order parameter, $q(z)$, (circles) and the hyperbolic tangent fit (turquoise line). Middle panel: the imposed thermal gradient required to maintain a fixed interfacial temperature of 225 K. Upper panel: the transverse velocity gradient (squares) that develops in response to an imposed momentum flux, along with the fit (green line). The vertical dotted lines indicate the locations of the Gibbs dividing surfaces of the two interfaces.

\AA) for the prismatic interfaces.³⁵ Over the range of shear rates investigated, $\sim 0.5 - 10.0 \text{ m s}^{-1}$, we find no significant differences in the interfacial widths for any of the crystal faces. All values of w_{10-90} obtained from shearing simulations fell inside the error bars of the values obtained from the quiescent simulations.

Table 2: Structural and dynamic properties of the interfaces of Ice-I_h with water.

Interface	$w_{10-90} (\text{\AA})$	$d_{10-90} (\text{\AA})$	$\kappa (\text{amu \AA}^{-2} \text{ fs}^{-1})$	$\rho_{sl} (\text{\AA}^{-2})$
Basal {0001}	7.5 ± 0.4	5 ± 1	0.31 ± 0.03	0.1227 ± 0.0003
Prismatic {10\bar{1}0}	7.2 ± 0.2	8 ± 2	0.48 ± 0.04	0.2014 ± 0.0005
Pyramidal {20\bar{2}1}	6.6 ± 0.2	6 ± 1	0.26 ± 0.02	0.0866 ± 0.0003
Secondary Prism {11\bar{2}0}	6.7 ± 0.2	7 ± 1	0.41 ± 0.02	0.1384 ± 0.0004

These values agree well with those reported by Haymet *et al.*^{39,44,54–57} Using a variety of water models and several different order parameters, they have estimated the ice / water interface to be between 5 \AA and 18 \AA depending on the particular interface and means of measure. For the SPC/E model, they found the basal and prismatic ice / water interface to be $\approx 11 \text{ \AA}$ wide from translational and window-averaged density order parameters. The interfacial widths were also estimated by observing the transition of a similar tetrahedral order parameter from their ice-like value of 0.9 to the bulk liquid value of 0.6. This gave estimates of $\approx 11 \text{ \AA}$, somewhat larger than our current estimates.

Solid-liquid friction at ice/water interfaces

In no-stick boundary conditions, fluid flowing over a solid is characterized by a slip length, δ , describing the extent of slip of the fluid at the interface. This length is the extrapolated distance from the interface where the tangential velocity component vanishes. For solids with weak interactions with the liquid, there is little drag imposed on the fluid and the resulting interfacial liquid velocity, Δv_{slip} , can be significant. In no-stick boundaries, therefore, the extrapolated slip lengths are also large (top panel of Fig. 4). Balasubramanian and Mundy have related the slip length to the

interfacial friction coefficient,

$$\lambda = \frac{\eta}{\delta} \quad (4)$$

where η is the shear viscosity of the liquid.⁶¹

For solids that have strong interactions with the liquid, a larger frictional drag is imposed on the fluid at the interface and the resulting slip lengths are smaller. When the solid-liquid interactions become large enough, the interface is best described with stick boundary conditions, and the slip length will vanish (middle panel of Fig. 4). Stick boundaries pose a problem for Eq. (4), as λ asymptotically goes to infinity as $\delta \rightarrow 0$. Likewise, some materials possess solid-liquid interactions that are strong enough for the extrapolated tangential velocity to vanish *before* reaching the solid. The velocity profile yields a negative slip length (bottom panel of Fig. 4, and the solid-liquid friction coefficient defined in Eq. (4) becomes meaningless. Ice shearing through liquid water is in the negative slip limit. The tangential velocity profile of the liquid extrapolates to zero several molecular layers before reaching the solid. Thus a new friction coefficient must be defined to describe these interfaces.

The solid-liquid friction coefficient may also be defined using the velocity drop across the interface, rather than the length scale over which this drop occurs. We can relate the imposed shear stress with the relative tangential velocity of the fluid in the interfacial region,⁴²

$$j_z(p_x) = \kappa \Delta v \quad (5)$$

where $\Delta v = v_x(\text{solid}) - v_x(\text{liquid})$ is the difference in transverse velocity between points that are unambiguously on the solid and liquid sides of the interface. In slip boundary conditions, κ and λ are identical, but Eq. (5) provides a direct analogy to non-equilibrium expressions for the interfacial thermal conductance (G),

$$J_z = G \Delta T. \quad (6)$$

Here, J_z is a thermal flux and the temperature drop is measured across an interface of *finite width*. By analogy, κ is a transport coefficient that measures interfacial momentum conductance.

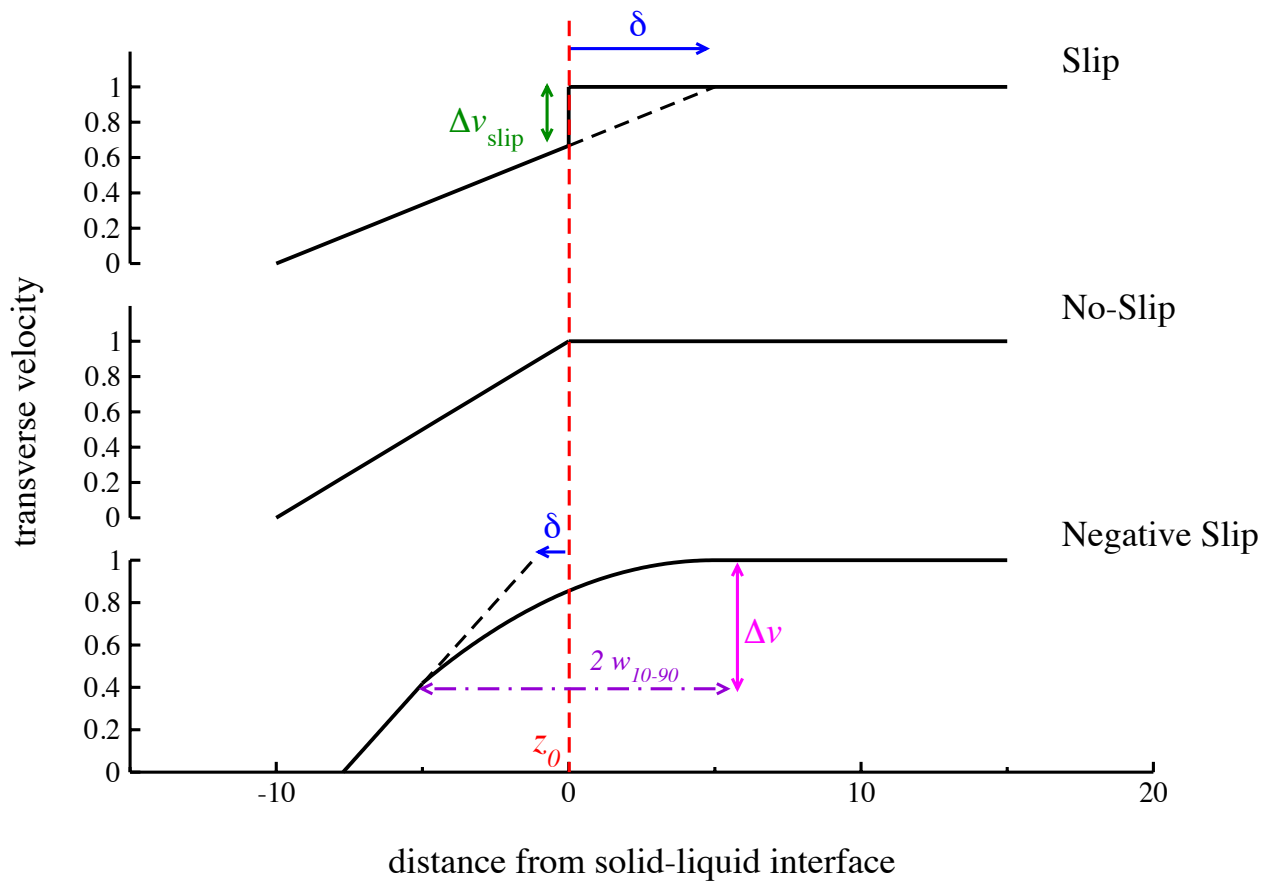


Figure 4: Transverse velocity profiles, $v_x(z)$, for interfaces in slip (top), no-slip (middle), and negative slip boundary conditions (bottom). The location of the interface is defined by a Gibbs dividing surface at z_0 . Under negative slip conditions, the 10-90 interfacial width, w_{10-90} , provides locations that are unambiguously on the liquid and solid sides of the interface.

In ice/water interfaces, the solid-liquid boundary is not an infinitely thin plane. An order parameter (the tetrahedrality) goes smoothly between the phases over a few molecular diameters. We can use this order parameter to find the interfacial width and define locations in space that are unambiguously on the solid and liquid sides of the interface. In what follows, we have used the Gibbs dividing surface (z_0) and the 10–90 width of the interface (w_{10-90}) to arrive at physical locations for measuring $v_x(\text{solid})$ and $v_x(\text{liquid})$. These uniquely define a friction coefficient in terms of well-defined structural features (z_0 and w_{10-90}) and dynamic properties ($v_x(z)$) of the interface.

Tangential velocity profiles from the simulations were fit using a piecewise function that is both continuous and continuously differentiable (see Supporting Information). To arrive at estimates of the interfacial velocities, these fits were queried at locations on either side of the structural Gibbs dividing surface,

$$v_x(\text{solid}) = v_x(z_0 + w_{10-90})$$

$$v_x(\text{liquid}) = v_x(z_0 - w_{10-90}).$$

The momentum flux, $j_z(p_x)$ is an imposed parameter of the VSS-RNEMD simulations, and by using Eq. (5), estimates of interfacial friction coefficient κ are straightforward.

The calculated κ values found for the four crystalline facets of ice-I_h investigated here are shown in Table 2. These results were found to be independent of the shear rate, as well as the direction of the shear relative to the features on the surfaces of the facets.

Note that the values of κ for the basal and prismatic crystal facets in Table 2 disagree with values for interfacial friction (λ) we previously reported.³⁵ In our initial report, the expression for the coefficient of friction was derived from equation (4) and the linear constitutive relation for shear stress in a bulk fluid. However, as described above, sheared ice/water interfaces are in the domain negative slip lengths. Eq. (4) should only be used in slip boundary conditions, as negative slip can yield coefficients of friction that appear to be smaller in magnitude than the zero slip conditions. In our previous work, the prismatic surface was found to have a larger negative slip length than the

basal face, indicating a prismatic surface that should have been reported with a larger coefficient of friction. If one instead uses Eq. (5) and interfacial widths to compute friction, the reported values come into agreement.

Dynamic measures of interfacial width under shear

The spatially-resolved orientational time correlation function,

$$C_2(z,t) = \langle P_2(\mathbf{u}_i(0) \cdot \mathbf{u}_i(t)) \delta(z_i(0) - z) \rangle, \quad (7)$$

provides local information about the decorrelation of molecular orientations in time. Here, P_2 is the second-order Legendre polynomial, and \mathbf{u}_i is the molecular unit vector that bisects the HOH angle of molecule i . The angle brackets indicate an average over all the water molecules and time origins, and the delta function restricts the average to specific regions in the z -dimension.

Recently, Laage and Hynes have determined the mechanism for water reorientation.^{62,63} Using molecular dynamics simulations, they found that water reorients by breaking a hydrogen bond with an overcoordinated first-shell neighbor, and makes a large angle jump to form a new hydrogen bond with an undercoordinated second-shell neighbor. The hydrogen bond cleavage and molecular reorientation occur in a concerted fashion, not in successive steps as was previously thought. With this detailed picture, they constructed the Extended Jump Model^{62,63} based on the Ivanov Jump Model and parameters extracted from their molecular simulations; the average jump amplitude of the rotational jump, θ_0 , and the frequency of the jumps, $1/\tau_0$. After accounting for molecular frame reorientation, the Extended Jump Model is able to predict reorientation relaxation times, τ_n^{jump} , which agree with experimental results as well as estimates obtained from simulations where fast librational motion is ignored.

In the ice crystal, decay of $C_2(z,t)$ is incomplete, while in the liquid, correlation times are typically measured in ps. Observing the spatial-transition between the decay regimes can define a dynamic measure of the interfacial width. To determine the dynamic widths of the interfaces under

shear, each of the systems were divided into bins along the z axis ($\approx 1 \text{ \AA}$ wide) and $C_2(z,t)$ was computed using only those molecules that were in the bin at the initial time. For each ice / water interface investigated, the following 0.5 ns simulations were computed: quiescent simulations (where no thermal or momentum gradient was present), simulations with only a thermal gradient present, and simulations where both thermal and momentum gradients were present. During these simulations, the positions and orientations of each molecule were recorded every 100 fs.

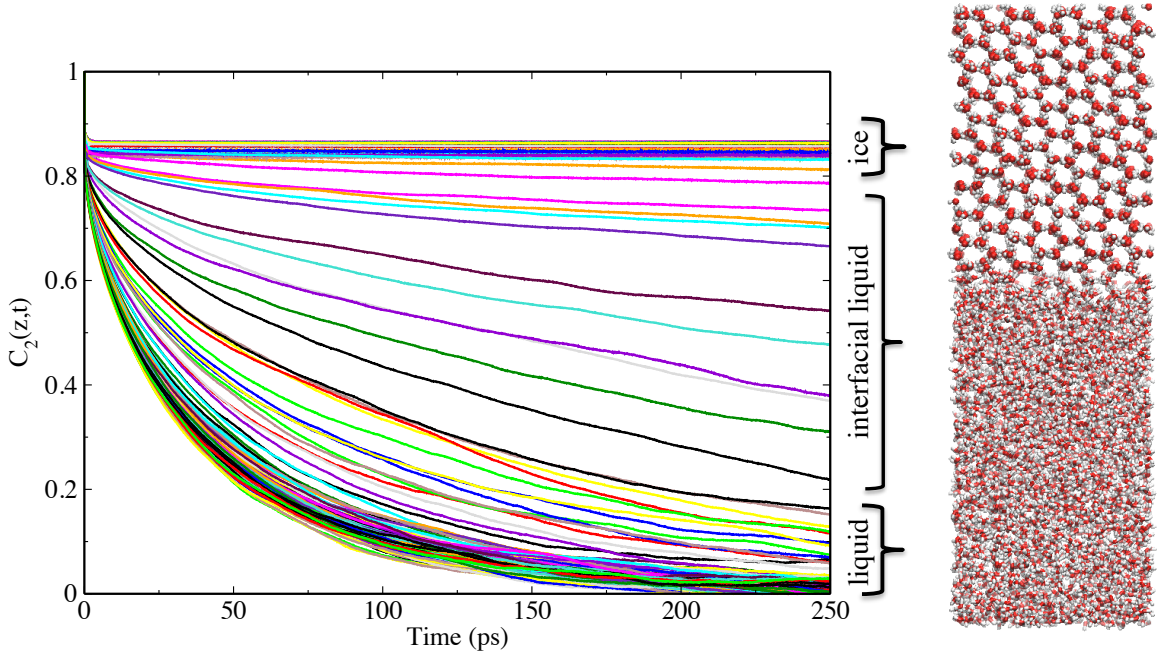


Figure 5: $C_2(z,t)$ collected in 1 \AA bins across the secondary prism ice/water interface. The band that experiences very little decay represents water molecules in the ice, while the band that decays quickly corresponds to bins in the liquid. The correlation function presents a continuous distribution of decay behaviors across the interface between ice and liquid water.

Computed $C_2(z,t)$ values have previously been fit to a triexponential decay, with three time constants: τ_{short} , measuring the librational motion of the water molecules, τ_{middle} , measuring the timescale for the large angle jumps during the breaking and making of hydrogen bonds, and τ_{long} ,

corresponding to the translational motion of the water molecules.³⁵ The Extended Jump Model also includes three similar decay constants, however two of them are linked and the dynamics of the decay is governed by two parameters. Since we are interested in how the decay times and the individual contributions may change through the interface, we have fit the $C_2(z,t)$ data with

$$C_2(z,t) = a e^{-t/\tau_{\text{short}}} + b e^{-t/\tau_{\text{middle}}} + (1 - a - b) e^{-t/\tau_{\text{long}}} \quad (8)$$

where all of the decay constants are considered local functions of the z coordinate. In Fig. 6, the z -coordinate profiles for the three decay constants, τ_{short} , τ_{middle} , and τ_{long} for the secondary prism interface is shown, along with their fractional components of the overall total decay, (a , b , $1 - a - b$), respectively. Similar figures for the other interfaces are provided in the Supporting Information.

In the liquid regions of all four interfaces, τ_{middle} and τ_{long} consistently approach 3 – 6 ps and 30 – 40 ps, respectively. Both of these times increase closer to the interface. Conversely, τ_{short} decreases from a liquid-state value of 72 – 76 fs approaching the interface.

The fractional contributions of the three motions to the overall decay changes as we approach the interface as well. Far from the ice, the librational motion and hydrogen bond breaking/making events each contribute to about 20 percent of the total decay, whereas frame reorientation contributes about 60 percent. As we approach the interface, the librations and hydrogen bond dynamics both decrease in contribution. The librations comprise approximately 15 percent of the overall decay at the edge of the interface, whereas the hydrogen bond contributions drop to approximately zero. In contrast, the fraction of the total decay due to frame reorientation is shown to increase approaching the interface. The time constant corresponding to this motion is seen to logarithmically increase as we approach the interface as the molecules become more ice-like. In the ice we would expect molecular reorientation to be incomplete, however, at the interface we observe frame reorientation to contribute 85 percent of the overall decay.

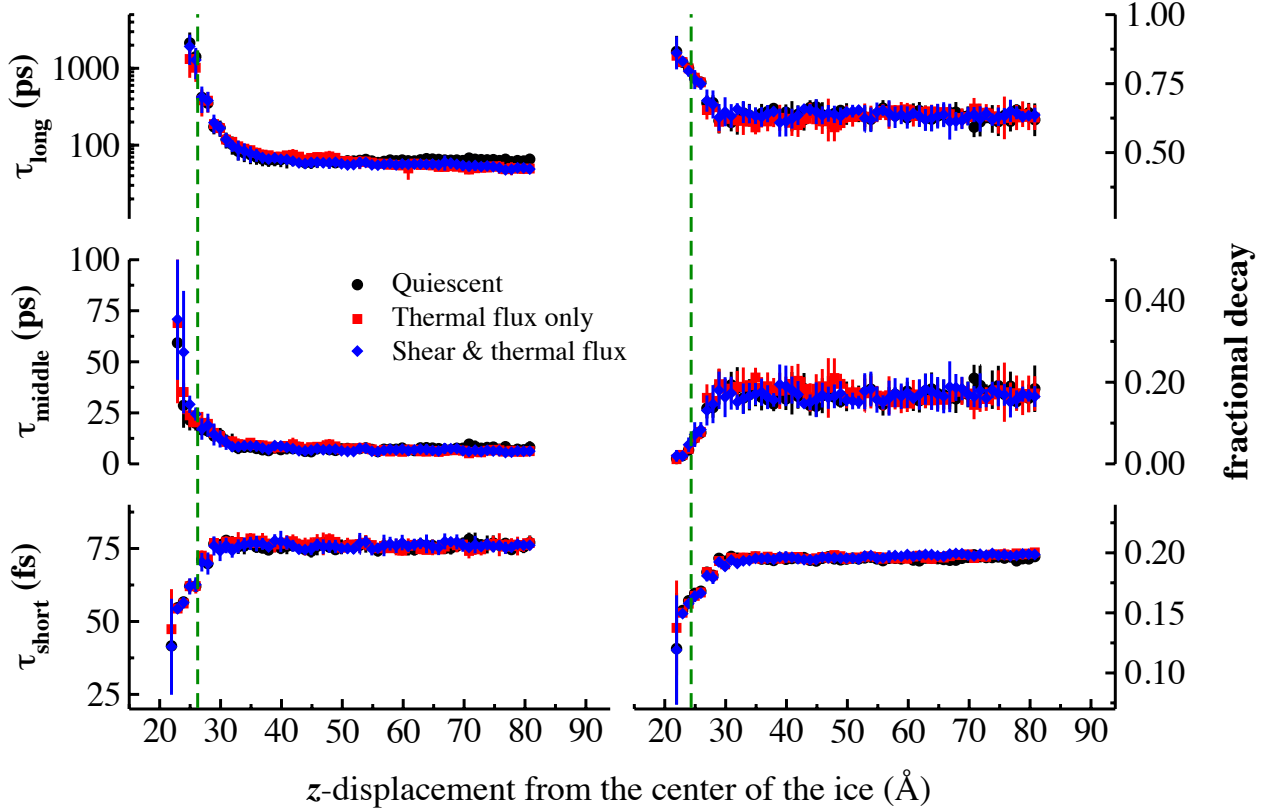


Figure 6: Decay times (left) for $C_2(z,t)$ at the secondary prism interface, and their fractional contributions to the overall decay (right) fit using Eq. (8). The local decay constants are plotted as a function of distance from the center of the ice slab. The vertical dashed line indicates the Gibbs dividing surface determined using the local tetrahedral order parameter. Results are shown for a quiescent system with no applied kinetic or momentum flux (black), an interface with an imposed kinetic energy flux (red), and a sheared simulation (blue) with both kinetic and momentum fluxes.

We have estimated a dynamic interfacial width by fitting the profiles of all the three orientational time constants with an exponential decay to the bulk-liquid behavior,

$$\tau(z) = \tau_{\text{liquid}} + (\tau_{\text{wall}} - \tau_{\text{liquid}})e^{-(z-z_0)/d} \quad (9)$$

where τ_{liquid} and τ_{wall} are the liquid and projected interfacial values of the decay constants, z_0 is the location of the Gibbs dividing surface, as measured by the structural order parameter. As with the structural widths, 10% – 90% dynamic widths are easily computed from the fits ($d_{10-90} = 2.197 d$). These values are provided in Table 2. All four interfaces exhibit dynamic widths that are $\sim 6 \text{ \AA}$,

and are in reasonable agreement with the structural widths above.

We note that Bryk and Haymet also calculated the orientational time correlation function at the basal interface of SPC/E water,³⁹ and observed the same qualitative trend through the ice / water interface, although the spatial resolution was not sufficient to resolve a dynamic width.

Laage and Hynes investigated how water molecules reorient around ions,^{64–67} proteins,⁶⁸ and in confined spaces.^{69,70} They also studied how the strength of the hydrogen bond might perturb the reorientation dynamics,⁷¹ and found the librational motion which forms a cone around the O-O vector is smaller for more strongly hydrogen bonded water. This may also provide a partial explanation for the increasing contribution of short time decay very close to the ice surfaces. Since the solid creates an excluded volume for the water molecules that are in proximity to the interface, the hindered range of motion (i.e., a smaller cone around the O-O vector) manifests as faster librational decay.

Discussion

The primary result of this paper is the observation that the different facets of ice-I_h produce significantly different solid-liquid interfacial friction coefficients with water (see Table 2). The two prismatic surfaces displayed the largest coefficients of friction, while the basal and pyramidal facets exhibited significantly lower friction.

The differences in friction are surprising given that densities and molecular interactions are identical for the four interfaces and the interfacial widths measured via both structural and dynamic features are also nearly the same. There are few remaining surface properties that could give rise to differences in solid-liquid friction of the four facets, notably surface corrugation and hydrogen bonding density at the interface. In this section we investigate the roles of these surface features.

Solid-liquid hydrogen bond density

One reason for the observed differences in friction coefficients is that ice surfaces may yield different densities of hydrogen bonds that bridge the solid and liquid. An ice surface that forms more hydrogen bonds with the interfacial liquid would be able to exert significant lateral forces on the liquid layer, yielding a larger friction coefficient. To probe this possibility, we have investigated the density of cross hydrogen bonds between the ice and the liquid.

Quantifying water molecules as “ice” or “liquid” at an interface of finite width requires a local order parameter for separating the molecules. We have again chosen the tetrahedral order parameter, q and the value of at the Gibbs dividing surface ($q(z_0) \approx 0.84$) as our partitioning criterion. Note that some molecules have strong tetrahedral ordering in the liquid phase, so this segregation will not yield perfect division between ice and liquid phase molecules.

To determine if a hydrogen bond has been formed between two water molecules, we used the geometric criteria of Luzar and Chandler.⁷² We identify a hydrogen bond between two water molecules if their oxygen sites are within $r_{OO} < 3.5$ Å and the OHO bond angle is within $\theta_{OHO} < 30$ degrees.

For each of the shearing simulations performed above, a hydrogen bond tetrahedrality matrix was constructed. Snapshots from the shearing trajectories were taken every 0.1 ps, and the tetrahedrality (q) value for each water molecule in the system was calculated. Hydrogen bonds were also identified, and the tetrahedrality of the donor (q_D) and acceptor (q_A) molecules were recorded. A probability density of hydrogen bonds categorized by donor and acceptor tetrahedrality, $\rho_{\text{HB}}(q_D, q_A)$, was then recorded.

The lower panel of Fig. 7 shows a hydrogen bond tetrahedrality distribution for the prismatic facet with q_D plotted along the x -axis and q_A along the y -axis. Population around $q_D \approx q_A \approx 0.9$ indicates the density of ice-ice hydrogen bonds in the system, while the liquid-state hydrogen bonds are concentrated in the lower left, and are significantly more diffuse. The off-diagonal regions of the distribution represent the population of molecules in tetrahedral (ice-like) environments bound to non-tetrahedral (liquid-like) environments. Integrating the population found in each of these regions and normalizing by the surface area of each ice crystal produces a surface density of hydrogen bonds (\AA^{-2}) formed between the ice and interfacial liquid,

$$\rho_{sl} = \frac{N_{\text{HB}}}{2L_x L_y} \left[\int_0^{0.84} dq_D \int_{0.84}^1 dq_A \rho_{\text{HB}}(q_D, q_A) + \int_0^{0.84} dq_A \int_{0.84}^1 dq_D \rho_{\text{HB}}(q_D, q_A) \right] \quad (10)$$

N_{HB} is the total number of hydrogen bonds found in the system, and L_x and L_y are the dimensions of the two ice facets exposed to the liquid. Values for ρ_{sl} for each of the ice surfaces are reported in Table 2.

The trend in surface density of solid-liquid hydrogen bonds reproduces the trend in the friction coefficients, indicating that friction at ice-I_h water interfaces is strongly influenced, if not governed, by the number of solid-liquid hydrogen bonds that can be formed. This result is robust under multiple shear rates and orientation of shear flow relative to the surface features of the ice, indicating that the hydrogen bonding statistics between an ice facet and the liquid are not altered by the imposed shear.

Surface corrugation

A second possible influence on the friction coefficient is the surface topography of the ice crystals, the dimensions of which are reported in Table 3. When a crystal of ice-I_h is cleaved along either of the two prismatic crystal facets, the exposed oxygen atoms present channel-like structures with channel widths of 6.35 Å and channel depths of 2.25 Å. When cleaved along the pyramidal facet, the resulting surface features a much larger channel, ~ 8.7 Å wide. Conversely, the basal surface

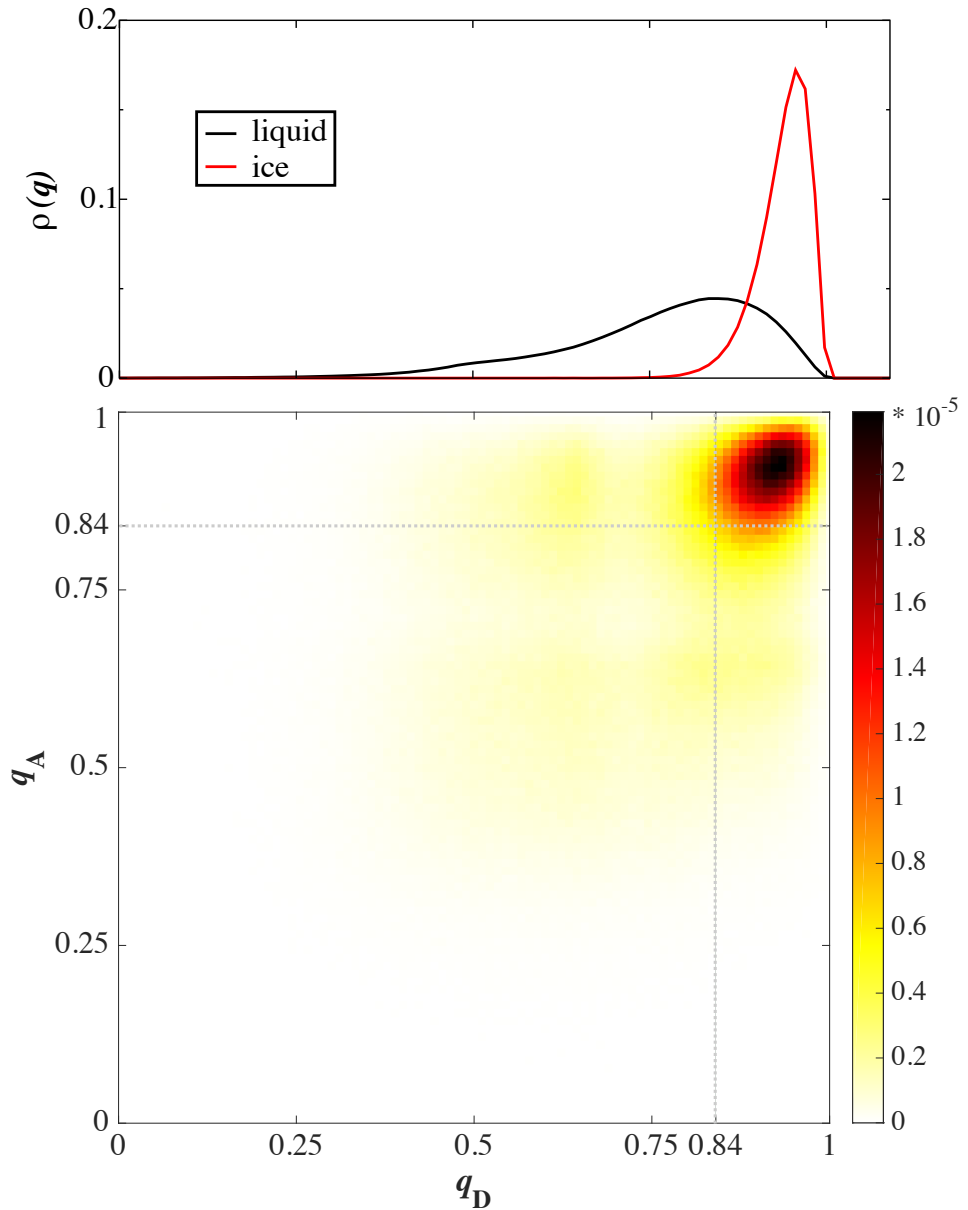


Figure 7: Distribution of hydrogen bonds at a prismatic interface showing the tetrahedralities of donor (q_D) and acceptor (q_A) molecules (lower panel). Distributions of tetrahedralities in bulk ice and liquid phases are shown in the upper panel, and the value of q at the Gibbs dividing surface is indicated with dashed lines. Hydrogen bonds between ice molecules are represented by the upper right square, while those between liquid molecules are in the lower left. Hydrogen bonds that bridge the ice-liquid interface exist primarily in the vertical and horizontal strips that remain.

presents a rather smooth surface to the liquid, with stripes of oxygen atoms forming surface ripples with depths of $\sim 1.3 \text{ \AA}$.

Table 3: Surface features of Ice-I_h facets.

Interface	Channel width (\AA)	Channel depth (\AA)
Basal {0001}	4.49	1.30
Prismatic {10\bar{1}0}	6.35	2.25
Pyramidal {20\bar{2}1}	8.65	2.59
Secondary Prism {11\bar{2}0}	6.35	2.25

The prismatic channels are quite stable. That is, we do not observe liquid phase molecules populating the prismatic and secondary prism surface channels. One might expect regions of low liquid density to yield smaller solid-liquid interactions, and it does appear that these two surfaces present roughly half of the surface oxygen atoms to the liquid. However, the molecules forming the bottoms of the channels are fully saturated (four hydrogen bonds each), while the molecules that form the tops of the channels present a high density of available hydrogen bond locations.

The oxygen-based surface features of the prism and secondary prism are identical, and only the orientation of the water molecules varies. This means that the patterning of donor and acceptors on the two facets is quite different. A liquid with internal hydrogen bonding constraints that is in contact with these facets will allow the prismatic surface to form a higher density of solid-liquid hydrogen bonds than the secondary prism, even with identical oxygen ordering at the interface.

In contrast with the prismatic facets, liquid state molecules do populate the surface channels on the pyramidal facet. Again, one might expect the interactions between the solid and the liquid in close physical contact to be quite large. However, the liquid molecules populating this channel do not pack efficiently and cannot fully saturate the surface locations available for hydrogen bonding, resulting in a lower solid-liquid hydrogen bond density and a smaller coefficient of friction.

With its smooth surface, one could make reasonable physical arguments for the basal face to have either high or low friction with liquid water. That is, liquid molecules should be able to form a fully populated network of hydrogen bonds with the surface, as there are no recessed surface molecules at the bottoms of deep channels, and no channel packing constraints. In the absence

of large surface undulations, however, liquid-phase molecules should also be able to slip over the surface easily. However, the basal facet was found to have an intermediate friction coefficient compared with the other facets studied here. The sensible explanation in light of the hydrogen bonding data is simply that the surface density of solid-liquid hydrogen bonds (however transitory) dominates the interfacial friction.

Conclusions

RNEMD simulations of the different facets of ice being drawn through surrounding water at the coexistence temperature indicate some facet-dependence of solid-liquid friction. We have defined a negative slip interfacial friction coefficient, κ (measured in amu \AA^{-2} fs $^{-1}$) and find that the two prismatic facets exert the largest drag on the surrounding liquid. The basal facet provides an intermediate level of drag, while the pyramidal facet has roughly half the interfacial friction of the prismatic facet.

Using the local tetrahedral order parameter as a metric to differentiate ice and liquid water molecules and a geometric hydrogen bonding criteria, the friction coefficients were shown to be largely governed by the surface density of solid-liquid hydrogen bonds (ρ_{sl}). A simple linear fit for the four interfaces yields

$$\kappa \approx 2.1772(\text{amu fs}^{-1}) \times \rho_{sl}(\text{\AA}^{-2}) + 0.0777(\text{amu \AA}^{-2} \text{ fs}^{-1}), \quad (11)$$

so the majority of the calculated solid-liquid friction is determined by the surface density of solid-liquid hydrogen bonds.

In addition, we have found the ice / water interfacial widths for all four crystal facets to be similar (using both structural and dynamic measures) and found these widths to be independent of shear rate. The similarity of interfacial width estimates for the four facets indicate that the particular facet of the exposed ice crystal has very little effect on how far into the bulk the ice-like structural ordering persists. While differences have been found in previous simulations of

ice / water interfaces,^{56,57} experimentally these differences have been less clear.⁷³ The significant differential friction coefficients obtained here suggest that while the liquid next to the ice might be structurally organized like bulk liquid, the dynamics of the molecules are still quite strongly perturbed by the ice. That is, the surface hydrogen bonding significantly alters how the water layers are pulled along with the ice during shear.

Acknowledgement

Support for this project was provided by the National Science Foundation under grant CHE-1362211 and CHE-1663773. Computational time was provided by the Center for Research Computing (CRC) at the University of Notre Dame.

Supporting Information Available

The fitting function used for the transverse velocity profiles, plots of the temperature, tetrahedrality, transverse velocity profiles, and orientational correlation functions for the interfaces not shown above, and regression analysis for the friction dependence on solid-liquid hydrogen bond density.

References

- (1) Bowden, F. P.; Hughes, T. P. The mechanism of sliding on ice and snow. *P. R. Soc. A* **1939**, *172*, 280–298.
- (2) Evans, D.; Nye, J.; Cheeseman, K. The kinetic friction of ice. *Proc. R. Soc. Lond. A* **1976**, *347*, 493–512.
- (3) Roberts, A. D.; Richardson, J. C. Interface study of rubber-ice friction. *Wear* **1981**, *67*, 55–69.
- (4) Derjaguin, B. V. Mechanical properties of the boundary lubrication layer. *Wear* **1988**, *128*, 19–27.
- (5) Liang, H.; Martin, J. M.; Mogne, T. L. Experimental investigation of friction on low-temperature ice. *Acta Mater.* **2003**, *51*, 2639–2646.
- (6) Higgins, D. D.; Marmo, B. A.; Jeffree, C. E.; Koutsos, V.; Blackford, J. R. Morphology of ice wear from rubber-ice friction tests and its dependence on temperature and sliding velocity. *Wear* **2008**, *265*, 634–644.
- (7) Oksanen, P.; Keinonen, J. The mechanism of friction of ice. *Wear* **1982**, *78*, 315–324.
- (8) Buhl, D.; Fauve, M.; Rhyner, H. The kinetic friction of polyethylen on snow: The influence of the snow temperature and the load. *Cold Reg. Sci. Technol.* **2001**, *33*, 133–140.
- (9) Bäurle, L.; Szabó, D.; Fauve, M.; Rhyner, H.; Spencer, N. D. Sliding friction of polyethylene on ice: Tribometer measurements. *Tribol. Lett.* **2006**, *24*, 77–84.
- (10) Bäurle, L.; Kaempfer, T. U.; Szabó, D.; Spencer, N. D. Sliding friction of polyethylene on snow and ice: Contact area and modeling. *Cold Reg. Sci. Technol.* **2007**, *47*, 276–289.
- (11) Calabrese, S. Frictional characteristics of materials sliding against ice. *Lubr. Eng.* **1980**, *36*, 283.

- (12) Kietzig, A. M.; Hatzikiriakos, S. G.; Englezos, P. Ice friction: The effects of surface roughness, structure, and hydrophobicity. *J. Appl. Phys.* **2009**, *106*, 024303.
- (13) Liang, H.; Martin, J. M.; Le Mogne, T. Friction-induced nonequilibrium phase transformation of low-temperature ice. *J. Appl. Phys.* **2005**, *97*, 043525.
- (14) Kietzig, A. M.; Hatzikiriakos, S. G.; Englezos, P. Physics of ice friction. *J. Appl. Phys.* **2010**, *107*, 081101.
- (15) Kennedy, F. E.; Schulson, E. M.; Jones, D. E. The friction of ice on ice at low sliding velocities. *Philos. Mag. A* **2000**, *80*, 1093–1110.
- (16) Maeno, N.; Arakawa, M. Adhesion shear theory of ice friction at low sliding velocities, combined with ice sintering. *J. Appl. Phys.* **2004**, *95*, 134–139.
- (17) Fortt, A.; Schulson, E. The resistance to sliding along Coulombic shear faults in ice. *Acta Mater.* **2007**, *55*, 2253–2264.
- (18) Fortt, A. L.; Schulson, E. M. Frictional sliding across Coulombic faults in first-year sea ice: A comparison with freshwater ice. *J. Geophys. Res.-Oceans* **2011**, *116*, 1–13.
- (19) Lishman, B.; Sammonds, P.; Feltham, D. A rate and state friction law for saline ice. *J. Geophys. Res.-Oceans* **2011**, *116*, 1–13.
- (20) Samadashvili, N.; Reischl, B.; Hynninen, T.; Ala-Nissilä, T.; Foster, A. S. Atomistic simulations of friction at an ice-ice interface. *Friction* **2013**, *1*, 242–251.
- (21) Kroes, G. J. Surface melting of the (0001) face of TIP4P ice. *Surf. Sci.* **1992**, *275*, 365–382.
- (22) Ikeda-Fukazawa, T.; Kawamura, K. Molecular-dynamics studies of surface of ice Ih. *J. Chem. Phys.* **2004**, *120*, 1395–1401.
- (23) Picaud, S. Dynamics of TIP5P and TIP4P/ice potentials. *J. Chem. Phys.* **2006**, *125*, 174712.

- (24) Conde, M. M.; Vega, C.; Patrykiejew, A. The thickness of a liquid layer on the free surface of ice as obtained from computer simulation. *J. Chem. Phys.* **2008**, *129*, 014702.
- (25) Bartels-Rausch, T.; Jacobi, H. W.; Kahan, T. F.; Thomas, J. L.; Thomson, E. S.; Abbatt, J. P. D.; Ammann, M.; Blackford, J. R.; Bluhm, H.; Boxe, C. et al. A review of air-ice chemical and physical interactions (AICI): liquids, quasi-liquids, and solids in snow. *Atmos. Chem. Phys.* **2014**, *14*, 1587–1633.
- (26) Sánchez, M. A.; Kling, T.; Ishiyama, T.; van Zadel, M.-J.; Bisson, P. J.; Mezger, M.; Jochum, M. N.; Cyran, J. D.; Smit, W. J.; Bakker, H. J. et al. Experimental and theoretical evidence for bilayer-by-bilayer surface melting of crystalline ice. *Proc. Natl. Acad. Sci. U.S.A.* **2017**, *114*, 227–232.
- (27) Pfalzgraff, W.; Neshyba, S.; Roeselova, M. Comparative molecular dynamics study of vapor-exposed basal, prismatic, and pyramidal surfaces of ice. *J. Phys. Chem. A* **2011**, *115*, 6184–6193.
- (28) Dash, J. G.; Fu, H.; Wettlaufer, J. S. The premelting of ice and its environmental consequences. *Rep. Prog. Phys.* **1995**, *58*, 115–167.
- (29) Rosenberg, R. Why is ice slippery? *Phys. Today* **2005**, *58*, 50–55.
- (30) Dash, J. G.; Rempel, A. W.; Wettlaufer, J. S. The physics of premelted ice and its geophysical consequences. *Rev. Mod. Phys.* **2006**, *78*, 695–741.
- (31) Malenkov, G. Liquid water and ices: understanding the structure and physical properties. *J. Phys.-Condensed Matter* **2009**, *21*, 283101.
- (32) Bhushan, B. *Introduction to Tribology*; John Wiley & Sons: New York, 2002.
- (33) Persson, B. N. J. Ice friction: Role of non-uniform frictional heating and ice premelting. *J. Chem. Phys.* **2015**, *143*, 224701.

- (34) Tuononen, A. J.; Kriston, A.; Persson, B.; Tuononen, A. J.; Kriston, A.; Persson, B. Multi-scale physics of rubber-ice friction. *J. Chem. Phys.* **2016**, *145*, 114703.
- (35) Louden, P.; Schoenborn, R.; Lawrence, C. P. Molecular dynamics simulations of the condensation coefficient of water. *Fluid Phase Equilibr.* **2013**, *349*, 83–86.
- (36) Buch, V.; Groenzin, H.; Li, I.; Shultz, M. J.; Tosatti, E. Proton order in the ice crystal surface. *Proc. Natl. Acad. Sci. U.S.A.* **2008**, *105*, 5969–5974.
- (37) Groenzin, H.; Li, I.; Buch, V.; Shultz, M. J. The single-crystal, basal face of ice Ih investigated with sum frequency generation. *J. Chem. Phys.* **2007**, *127*, 214502.
- (38) Hirsch, T. K.; Ojamäe, L. Quantum-chemical and force-field investigations of ice Ih: Computation of proton-ordered structures and prediction of their lattice energies. *J. Phys. Chem. B* **2004**, *108*, 15856–15864.
- (39) Bryk, T.; Haymet, A. D. J. Ice 1h/water interface of the SPC/E model: Molecular dynamics simulations of the equilibrium basal and prism interfaces. *J. Chem. Phys.* **2002**, *117*, 10258–10268.
- (40) Berendsen, H. J. C.; Grigera, J. R.; Straatsma, T. P. The Missing Term in Effective Pair Potentials. *J. Phys. Chem.* **1987**, *91*, 6269–6271.
- (41) Arbuckle, B. W.; Clancy, P. Effects of the Ewald sum on the free energy of the extended simple point charge model for water. *J. Chem. Phys.* **2002**, *116*, 5090–5098.
- (42) Kuang, S.; Gezelter, J. D. Velocity shearing and scaling RNEMD: a minimally perturbing method for simulating temperature and momentum gradients. *Mol. Phys.* **2012**, *110*, 691–701.
- (43) Báez, L. A.; Clancy, P. Phase equilibria in extended simple point charge ice-water systems. *J. Chem. Phys.* **1995**, *103*, 9744–9755.

- (44) Bryk, T.; Haymet, A. D. J. The Ice/Water Interface: DensityTemperature Phase Diagram for the SPC/E Model of Liquid Water. *Mol. Simulat.* **2004**, *30*, 131–135.
- (45) Sanz, E.; Vega, C.; Abascal, J. L. F.; MacDowell, L. G. Phase diagram of water from computer simulation. *Phys. Rev. Lett.* **2004**, *92*, 255701.
- (46) Fennell, C. J.; Gezelter, J. D. Computational free energy studies of a new ice polymorph which exhibits greater stability than ice Ih. *J. Chem. Theory Comput.* **2005**, *1*, 662–667.
- (47) Gay, S. C.; Smith, E. J.; Haymet, A. D. J. Dynamics of melting and stability of ice 1h: Molecular-dynamics simulations of the SPC/E model of water. *J. Chem. Phys.* **2002**, *116*, 8876–8880.
- (48) García Fernández, R.; Abascal, J. L. F.; Vega, C. The melting point of ice Ih for common water models calculated from direct coexistence of the solid-liquid interface. *J. Chem. Phys.* **2006**, *124*, 144506.
- (49) Abascal, J. L. F.; García Fernández, R.; MacDowell, L. G.; Sanz, E.; Vega, C. Ice: A fruitful source of information about liquid water. *J. Mol. Liq.* **2007**, *136*, 214–220.
- (50) Vrbka, L.; Jungwirth, P. Molecular dynamics simulations of freezing of water and salt solutions. *J. Mol. Liq.* **2007**, *134*, 64–70.
- (51) Meineke, M. A.; Vardeman, C. F.; Lin, T.; Fennell, C. J.; Gezelter, J. D. OOPSE: An Object-Oriented Parallel Simulation Engine for Molecular Dynamics. *J. Comput. Chem.* **2005**, *26*, 252–271.
- (52) Gezelter, J. D.; Bhattacharai, H.; Niedhart, S.; Louden, P. B.; Lin, T.; Vardeman, C. F.; Fennell, C. J.; Meineke, M. A.; Kuang, S.; Lamichane, M. et al. OpenMD, an Open Source Engine for Molecular Dynamics. 2016; <http://openmd.org>.
- (53) Fennell, C. J.; Gezelter, J. D. Is the Ewald summation still necessary? Pairwise alternatives to the accepted standard for long-range electrostatics. *J. Chem. Phys.* **2006**, *124*, 234104.

- (54) Karim, O. A.; Haymet, A. D. J. The ice/water interface: A molecular dynamics simulation study. *J. Chem. Phys.* **1988**, *89*, 6889–6896.
- (55) Karim, O. A.; Kay, P. A.; Haymet, A. D. J. The ice/water interface: A molecular dynamics simulation using the simple point charge model. *J. Chem. Phys.* **1990**, *92*, 4634.
- (56) Hayward, J. A.; Haymet, A. D. J. Ice/water interface: molecular dynamics simulations of the basal, prism, {2021}, and {2110} interfaces of ice Ih. *J. Chem. Phys.* **2001**, *114*, 3713–3726.
- (57) Hayward, J. A.; Haymet, A. D. J. The ice/water interface: orientational order parameters for the basal, prism, {2021}, and {2110} interfaces of ice Ih. *Phys. Chem. Chem. Phys.* **2002**, *4*, 3712–3719.
- (58) Chau, P.-L.; Hardwick, A. J. A new order parameter for tetrahedral configurations. *Mol. Phys.* **1998**, *93*, 511–518.
- (59) Errington, J.; Debenedetti, P. Relationship between structural order and the anomalies of liquid water. *Nature* **2001**, *409*, 318–321.
- (60) Kumar, P.; Buldyrev, S. V.; Stanley, H. E. A tetrahedral entropy for water. *Proc. Natl. Acad. Sci. U.S.A.* **2009**, *106*, 22130–22134.
- (61) Balasubramanian, S.; Mundy, C. J. Calculation of friction coefficient of a solid-liquid interface via a non-equilibrium molecular dynamics simulation. *Bull. Mater. Sci.* **1999**, *22*, 873–876.
- (62) Laage, D.; Hynes, J. T. A Molecular Jump Mechanism of Water Reorientation. *Science* **2006**, *311*, 832–835.
- (63) Laage, D.; Hynes, J. T. On the molecular mechanism of water reorientation. *J. Phys. Chem. B* **2008**, *112*, 14230–14242.
- (64) Laage, D.; Hynes, J. T. Reorientational dynamics of water molecules in anionic hydration shells. *Proc. Natl. Acad. Sci. U.S.A.* **2007**, *104*, 11167–11172.

- (65) Laage, D.; Hynes, J. T. On the Residence Time for Water in a Solute Hydration Shell : Application to Aqueous Halide Solutions. *J. Phys. Chem. B* **2008**, *112*, 7697–7701.
- (66) Stirnemann, G.; Sterpone, F.; Laage, D. Dynamics of water in concentrated solutions of amphiphiles: Key roles of local structure and aggregation. *J. Phys. Chem. B* **2011**, *115*, 3254–3262.
- (67) Laage, D.; Stirnemann, G.; Sterpone, F.; Rey, R.; Hynes, J. T. Reorientation and Allied Dynamics in Water and Aqueous Solutions. *Annu. Rev. Phys. Chem.* **2011**, *62*, 395–416.
- (68) Duboué-Dijon, E.; Laage, D. Comparative study of hydration shell dynamics around a hyperactive antifreeze protein and around ubiquitin. *J. Chem. Phys.* **2014**, *141*, 22D529.
- (69) Laage, D.; Thompson, W. H. Reorientation dynamics of nanoconfined water: Power-law decay, hydrogen-bond jumps, and test of a two-state model. *J. Chem. Phys.* **2012**, *136*, 044513.
- (70) Fogarty, A. C.; Coudert, F. X.; Boutin, A.; Laage, D. Reorientational dynamics of water confined in zeolites. *Chem. Phys. Chem.* **2014**, *15*, 521–529.
- (71) Laage, D.; Hynes, J. T. Do more strongly hydrogen-bonded water molecules reorient more slowly? *Chem. Phys. Lett.* **2006**, *433*, 80–85.
- (72) Luzar, A.; Chandler, D. Hydrogen-bond kinetics in liquid water. *Nature* **1996**, *379*, 55.
- (73) Beaglehole, D.; Wilson, P. Thickness and anisotropy of the ice-water interface. *J. Phys. Chem.* **1993**, *97*, 11053–11055.

Graphical TOC Entry

